

# A Multidimensional Relativistic Hydrodynamics Code with a General Equation of State

Eunwoo Choi<sup>1</sup> and Paul J. Wiita<sup>2,3</sup>

## ABSTRACT

The ideal gas equation of state with a constant adiabatic index, although commonly used in relativistic hydrodynamics, is a poor approximation for most relativistic astrophysical flows. Here we propose a new general equation of state for a multi-component relativistic gas which is consistent with the Synge equation of state for a relativistic perfect gas and is suitable for numerical (special) relativistic hydrodynamics. We also present a multidimensional relativistic hydrodynamics code incorporating the proposed general equation of state, based on the HLL scheme, which does not make use of a full characteristic decomposition of the relativistic hydrodynamic equations. The accuracy and robustness of this code is demonstrated in multidimensional calculations through several highly relativistic test problems taking into account nonvanishing tangential velocities. Results from three-dimensional simulations of relativistic jets show that the morphology and dynamics of the relativistic jets are significantly influenced by the different equation of state and by different compositions of relativistic perfect gases. Our new numerical code, combined with our proposed equation of state is very efficient and robust, and unlike previous codes, it gives very accurate results for thermodynamic variables in relativistic astrophysical flows.

*Subject headings:* equation of state — galaxies: jets — hydrodynamics — methods: numerical — relativity — shock waves

---

<sup>1</sup>Department of Astronomy and Atmospheric Sciences, Kyungpook National University, Daegu 702-701, Korea; echoi@knu.ac.kr

<sup>2</sup>Department of Physics and Astronomy, Georgia State University, P.O. Box 4106, Atlanta, GA 30302-4106, USA

<sup>3</sup>Department of Physics, The College of New Jersey, P.O. Box 7718, Ewing, NJ 08628, USA

## 1. Introduction

Many high energy astrophysical phenomena, including accretion flows, jet flows, gamma-ray bursts, and pulsar winds involve relativistic flows. In powerful extragalactic radio sources, for example, ejections from galactic nuclei produce intrinsic beam Lorentz factors of usually more than 5 and apparently up to  $\sim 50$ , which are required to explain the apparent superluminal motions observed in extragalactic radio sources associated with active galactic nuclei (e.g., Lister et al. 2009). In the expansion of many relativistic jets the internal thermal energy of a gas is converted into bulk kinetic energy so as to reach a high Lorentz factor in a short distance. Then this kinetic energy is dissipated by shock interactions, mostly by terminal shock complexes, and partially by internal shocks within the jets as they propagate over long distances (e.g., Norman et al. 1982). Since relativistic flows are inherently non-linear and complex, in addition to possessing large Lorentz factors, numerical simulations have been performed to investigate such relativistic flows, for example, in the propagation of relativistic extragalactic jets (e.g., Duncan & Hughes 1994; Martí et al. 1997; Rosen et al. 1999; Hughes et al. 2002; Choi et al. 2007).

Many explicit finite difference schemes originally applied to classical hydrodynamics have been employed to treat special relativistic hydrodynamics numerically. These schemes to solve the relativistic hydrodynamic equations are based on either exact or approximate solutions to the local Riemann problem (Schneider et al. 1993; Falle & Komissarov 1996; Donat et al. 1998; Aloy et al. 1999; Del Zanna & Bucciantini 2002; Anninos & Fragile 2003; Mignone & Bodo 2005; Mignone et al. 2005). Some of these schemes adopt local characteristic decomposition of the Jacobian matrix to build numerical fluxes. It is often difficult to build characteristic decomposition in some regimes, especially in ultrarelativistic limits, due to the degeneracy of the characteristic information. Thus the use of an alternative scheme becomes sensible when the characteristic decomposition is unknown. The HLL scheme proposed by Harten et al. (1983) for classical hydrodynamics is based on an approximate Riemann solver that does not require full, and numerically expensive, characteristic decomposition. This feature of the HLL scheme makes its use very attractive, especially in multidimensions, where computational efficiency and robustness is extremely important. This scheme was applied first to relativistic hydrodynamics by Schneider et al. (1993) in one dimension and by Duncan & Hughes (1994) in multidimensions.

It is worth stressing that many treatments of relativistic astrophysical problems have assumed a ideal gas equation of state with a constant polytropic index, but this is a reasonable approximation only if the gas is either strictly subrelativistic or ultrarelativistic. However, when the gas is semirelativistic or when the gas has two components, e.g., nonrelativistic protons and relativistic electrons, this assumption is no longer correct. This was shown for

the relativistic perfect gas law by Synge (1957), where the exact form of an equation of state relating thermodynamic quantities of specific enthalpy and temperature is completely described in terms of modified Bessel functions.

Since the correct equation of state for the relativistic perfect gas has been recognized as being important, several investigations with a more general equation of state have been reported in numerical relativistic hydrodynamics. Falle & Komissarov (1996) described an upwind numerical code for special relativistic hydrodynamics with the Synge equation of state for multi-component relativistic gas. More recently, Mignone et al. (2005) used, in their upwind relativistic hydrodynamic code, a simple equation of state that closely approximates the Synge equation of state for a single-component relativistic gas. Several numerical simulations in the context of relativistic extragalactic jets make use of the general equation of state to account for transitions from nonrelativistic to relativistic temperature (Komissarov & Falle 1998; Scheck et al. 2002; Perucho & Martí 2007; Meliani et al. 2008; Rossi et al. 2008). Scheck et al. (2002) used the Synge equation of state for different compositions, including pure leptonic and baryonic plasmas, to investigate the influence of the composition of relativistic extragalactic jets on their long-term evolution. Similarly, Meliani et al. (2008) studied the relativistic extragalactic jet deceleration through density discontinuities by using the Synge-like equation of state with a variable polytropic index.

In this work we propose an analytical form of equation of state for the multi-component relativistic perfect gas that is consistent with the Synge equation of state in the relativistic regime. This proposed equation of state is suitable for a numerical code from the computational point of view, unlike the Synge equation of state, which involves the computation of Bessel functions. We then build a multidimensional relativistic hydrodynamics code based on the HLL scheme using the proposed equation of state, and demonstrate the accuracy and robustness of this code by presenting several test problems and numerical simulations. In particular, we plan to use this code to simulate relativistic extragalactic jets that are probably composed of a mixture of relativistic particles of different masses. Numerical simulations of relativistic jets of different compositions are challenging, but are made tractable by using the proposed equation of state that accounts for different compositions of relativistic gas.

This paper is organized as follows. In §2 we present the equations of motion and the Synge equation of state, and we describe the proposed general equation of state for the relativistic gas. In §3 we describe a relativistic hydrodynamics code based on the HLL scheme, incorporating this proposed equation of state. In §§4 and 5 we present numerical tests and simulations with the code to demonstrate the performance of the code. A conclusion is given in §6.

## 2. Relativistic Hydrodynamics

### 2.1. Equations of Motion

The motion of relativistic gas is described by a system of conservation equations. The equations in special relativistic hydrodynamics are written in a covariant form (Landau & Lifshitz 1959; Wilson & Mathews 2003) as

$$\partial_\alpha (\rho U^\alpha) = 0, \quad (1)$$

$$\partial_\alpha (\rho h U^\alpha U^\beta + p g^{\alpha\beta}) = 0. \quad (2)$$

Here,  $\partial_\alpha = \partial/\partial x^\alpha$  is the covariant derivative with respect to spacetime coordinates  $x^\alpha = [t, x_j]$ ,  $U^\alpha = [\Gamma, \Gamma v_j]$  is the normalized ( $U^\alpha U_\alpha = -1$ ) four-velocity vector, where  $\Gamma$  is the Lorentz factor, and  $g^{\alpha\beta} = \text{diag}\{-1, 1, 1, 1\}$  is the metric tensor in Minkowski space. The speed of light is set to unity ( $c = 1$ ) in this work. Greek indices (e.g.,  $\alpha, \beta$ ) denote the spacetime components while Latin indices (e.g.,  $i, j$ ) indicate the spatial components. The rest mass density, specific enthalpy, and pressure in the local rest frame are denoted by  $\rho$ ,  $h$ , and  $p$ , respectively.

In Cartesian coordinates these relativistic hydrodynamic equations can be written in conservative form as

$$\frac{\partial \mathbf{q}}{\partial t} + \frac{\partial \mathbf{F}_x}{\partial x} + \frac{\partial \mathbf{F}_y}{\partial y} + \frac{\partial \mathbf{F}_z}{\partial z} = 0, \quad (3)$$

where  $\mathbf{q}$  is the state vector of conservative variables and  $\mathbf{F}_x$ ,  $\mathbf{F}_y$ , and  $\mathbf{F}_z$  are respectively the flux vectors in the  $x$ ,  $y$ , and  $z$ -directions, defined by

$$\mathbf{q} = \begin{bmatrix} D \\ M_x \\ M_y \\ M_z \\ E \end{bmatrix}, \quad \mathbf{F}_x = \begin{bmatrix} D v_x \\ M_x v_x + p \\ M_y v_x \\ M_z v_x \\ (E + p) v_x \end{bmatrix}. \quad (4)$$

The flux vectors  $\mathbf{F}_y$  and  $\mathbf{F}_z$  are given by properly permuting indices. The conservative variables  $D$ ,  $M_x$ ,  $M_y$ ,  $M_z$ , and  $E$  represent respectively the mass density, three components of momentum density, and energy density in the reference frame.

The variables in the reference frame are nonlinearly coupled to those in the local rest frame via the transformations

$$D = \Gamma \rho, \quad (5)$$

$$M_x = \Gamma^2 \rho h v_x, \quad M_y = \Gamma^2 \rho h v_y, \quad M_z = \Gamma^2 \rho h v_z, \quad (6)$$

$$E = \Gamma^2 \rho h - p, \quad (7)$$

where the Lorentz factor is given by  $\Gamma = 1/\sqrt{1 - v^2}$  with  $v^2 = v_x^2 + v_y^2 + v_z^2$ .

## 2.2. Equation of State

The system of conservation equations describing the motion of relativistic gas is completed with an equation of state that relates the thermodynamic quantities of specific enthalpy, rest mass density, and pressure. In general the equation of state can be expressed with the specific enthalpy expressed as a function of the rest mass density and the pressure

$$h = h(\rho, p). \quad (8)$$

The sound speed  $c_s$  is then defined as

$$c_s^2 = \frac{\rho}{h} \frac{\partial h}{\partial \rho} \left( 1 - \rho \frac{\partial h}{\partial p} \right)^{-1}. \quad (9)$$

The explicit form of the sound speed depends on the particular choice of the equation of state.

The exact form of equation of state for a relativistic perfect gas composed of multiple components was derived by Synge (1957). For a single-component relativistic gas the equation of state is written as

$$h = \frac{K_3(\xi)}{K_2(\xi)}, \quad (10)$$

where  $K_2$  and  $K_3$  are respectively the modified Bessel function of the orders two and three and  $\xi = \rho/p$  is a measure of inverse temperature. Under the Synge equation of state a relativistic perfect gas is entirely described in terms of the modified Bessel functions. The Synge equation of state for a relativistic gas can be written in the form

$$h = 1 + \frac{\gamma_r^*}{\gamma_r^* - 1} \frac{p}{\rho}, \quad (11)$$

where the quantity  $\gamma_r^*$  is defined by

$$\gamma_r^* = \frac{h - 1}{h - 1 - \xi^{-1}}. \quad (12)$$

Then the sound speed is written as

$$c_s^2 = \frac{\gamma_r p}{\rho h}, \quad (13)$$

and the relativistic adiabatic index  $\gamma_r$  is given by

$$\gamma_r = \frac{h' \xi^2}{h' \xi^2 + 1}, \quad (14)$$

where  $h' = dh/d\xi$ . The quantities  $\gamma_r^*$  and  $\gamma_r$  are constant and equal if the gas remains ultrarelativistic or subrelativistic (i.e.,  $\gamma_r^* = \gamma_r = 4/3$  for  $\xi \ll 1$  or  $5/3$  for  $\xi \gg 1$ ). For

the intermediate regime  $\gamma_r^*$  and  $\gamma_r$  vary slightly differently between the two limiting cases (Falle & Komissarov 1996).

For a multi-component relativistic gas, the direct use of the Synge equation of state involves the computation of Bessel functions, thus requires significant computation cost and results in computational inefficiency. Here we propose a new general equation of state for multi-component relativistic gas that uses analytical expression and is more efficient and suitable for numerical computations. We suppose that the relativistic gas is composed of electrons, positrons, and protons although more components of relativistic gas easily can be considered. The total number density  $n$  is then given by

$$n = \sum n_i = n_{e-} + n_{e+} + n_{p+}, \quad (15)$$

where  $n_{e-}$ ,  $n_{e+}$ , and  $n_{p+}$  are the electron, positron, and proton number densities, respectively. We ignore the production or annihilation of electron-positron pairs and assume the composition of electrons, positrons, and protons is maintained. The assumption of charge neutrality gives us the relations  $n_{e-} = n_{e+} + n_{p+}$  and  $n = 2n_{e-}$ . The total rest mass density and pressure are respectively given by  $\rho = \sum \rho_i = \sum n_i m_i$  and  $p = \sum p_i = \sum n_i kT$ , where  $k$  is the Boltzmann constant and  $T$  is the temperature.

For our equation of state for multi-component relativistic gas we adopt the equation of state, previously introduced by Mathews (1971) and later used by Meliani et al. (2004), which closely reproduces the Synge equation of state for a single-component relativistic gas (Mignone et al. 2005). The equation of state takes the form

$$\frac{p}{\rho} = \frac{1}{3} \left( \frac{e}{\rho} - \frac{\rho}{e} \right), \quad (16)$$

where  $e$  is the energy density in the local rest frame. It can be solved for the specific enthalpy using  $\rho h = e + p$  as

$$h = \frac{5}{2} \frac{p}{\rho} + \sqrt{\frac{9}{4} \left( \frac{p}{\rho} \right)^2 + 1}. \quad (17)$$

For a multi-component relativistic gas, the total enthalpy is then given by  $\rho h = \sum \rho_i h_i = \sum [(5/2)n_i kT + \sqrt{(9/4)(n_i kT)^2 + (n_i m_i)^2}]$ . After we express the total enthalpy in terms of each component, we can eliminate  $n_{e+}$  using the above relations given in the charge neutrality assumption. Our proposed equation of state is obtained by simplifying the expression of the total enthalpy. We find the resulting equation of state for a multi-component relativistic gas to be

$$h = \frac{5}{2} \frac{1}{\xi} + (2 - \chi) \left[ \frac{9}{16} \frac{1}{\xi^2} + \frac{1}{(2 - \chi + \chi\mu)^2} \right]^{1/2} + \chi \left[ \frac{9}{16} \frac{1}{\xi^2} + \frac{\mu^2}{(2 - \chi + \chi\mu)^2} \right]^{1/2}, \quad (18)$$

where  $\chi = n_{p+}/n_{e-}$  is the relative fraction of proton and electron number densities and  $\mu = m_p/m_e$  is the mass ratio of proton to electron. We note that  $\chi = 0$  represents an electron-positron gas while  $\chi = 1$  indicates an electron-proton gas. The proposed equation of state reduces to the equation of state in equation (17) when the electron-positron gas ( $\chi = 0$ ) is considered. This proposed equation of state holds only in the limit where the composition of the plasma is fixed in space and time. In reality, however, the plasma composition may change through fluid mixing or the creation or annihilation of electron-positron pairs, either of which can alter the equation of state by effectively changing  $\chi$  in different regions of the fluid. Nonetheless, this assumption of constant  $\chi$  is a useful first order approximation in many situations.

Using the proposed equation of state we show in Figure 1 the relativistic adiabatic indices,  $\gamma_r$ , as functions of inverse temperature  $\xi$ , for several different compositions of the relativistic gas. Compositions of  $\chi = 0, 0.1, 0.3, 0.6$ , and 1 are shown. The value of  $\gamma_r$  critically depends on the composition of the relativistic gas as protons become relativistic at a much higher temperature than do electrons. Different proton fractions cause the adiabatic index to vary substantially at intermediate temperatures. For electron-positron and electron-proton gases, we compare  $\gamma_r$  values from our equation of state with  $\gamma$  values from the Synge equation of state as given in Figure 1 of Falle & Komissarov (1996). Direct measurements of relative errors give  $|\gamma_r - \gamma|/\gamma \lesssim 0.4\%$  for an electron-positron gas and  $\lesssim 0.3\%$  for an electron-proton gas.

Figure 2 shows the quantities  $\gamma_r^*$ , specific enthalpy  $h$ , and sound speed  $c_s$ , as functions of inverse temperature  $\xi$ , for different equations of state. Results are shown for the ideal gas equation of state with fixed adiabatic indices of  $\gamma = 5/3$  and  $4/3$  as well as for the proposed general equation of state for pure electron-positron and pure electron-proton gases. The thermodynamic quantities computed using the proposed general equation of state asymptotically approach those computed using the ideal gas equation of state with  $\gamma = 4/3$  in the hot gas limit ( $\xi \ll 1$ ) and  $\gamma = 5/3$  in the cold gas limit ( $\xi \gg 1$ ). For intermediate regimes the thermodynamic quantities vary between those two limiting cases, depending on the composition of the relativistic gas.

### 3. Numerical Scheme

We now describe a relativistic hydrodynamics code incorporating the proposed equation of state for a relativistic perfect gas, based on the HLL scheme originally proposed by Harten et al. (1983) for classical hydrodynamics. The HLL scheme avoids a full characteristic decomposition of the relativistic hydrodynamic equations and uses an approximate solution

to the Riemann problem where the two constant states separated by the middle contact wave are averaged into a single intermediate state. The HLL scheme requires accurate estimates of the maximum and minimum wave speeds for the solution of the Riemann problem. In classical hydrodynamics Einfeldt (1988) proposed good ways to estimate the wave speeds based on the maximum and minimum eigenvalues of the Jacobian matrix.

The wave speeds needed in our formulation for relativistic flows can be similarly estimated from the maximum and minimum eigenvalues  $a_x^\pm$  of the Jacobian matrix,  $A_x = \partial \mathbf{F}_x(\mathbf{u}) / \partial \mathbf{q}(\mathbf{u})$ , where  $\mathbf{u} = [\rho, v_x, v_y, v_z, p]^T$  is the state vector of primitive variables, and

$$a_x^\pm = \frac{(1 - c_s^2) v_x \pm \sqrt{(1 - v^2) c_s^2 [1 - v^2 c_s^2 - (1 - c_s^2) v_x^2]}}{1 - v^2 c_s^2}. \quad (19)$$

The maximum and minimum eigenvalues are based on a simple application of the relativistic addition of velocity components decomposed into coordinates directions and simply reduce to  $a_x^\pm = (v_x \pm c_s) / (1 \pm v_x c_s)$  in the one-dimensional case.

Numerical integration of relativistic hydrodynamic equations advances by evolving the state vector of conservative variables in time. However, in order to compute the flux vectors for the evolution, the primitive variables  $\mathbf{u}$  involved in the flux vectors should be recovered from the conservative variables  $\mathbf{q}$  at each time step by the inverse transformation

$$\rho = \frac{D}{\Gamma}, \quad (20)$$

$$v_x = \frac{M_x}{E + p}, \quad v_y = \frac{M_y}{E + p}, \quad v_z = \frac{M_z}{E + p}, \quad (21)$$

$$p = \Gamma D h - E. \quad (22)$$

The inverse transformation is nonlinearly coupled and reduces to a single equation for the pressure

$$f(p) = \Gamma(p) D h(\xi(p)) - E - p = 0. \quad (23)$$

This nonlinear equation can be solved numerically using a Newton-Raphson iterative method in which the derivative of the equation with respect to pressure is given by

$$\frac{df}{dp} = \frac{d\Gamma}{dp} D h + \Gamma D \frac{dh}{d\xi} \frac{d\xi}{dp} - 1. \quad (24)$$

Once the pressure is found numerically, the rest mass density and velocity are recovered by the inverse transformation. This procedure of inversion from conservative to primitive variables is valid for a general equation of state by specifying the expression of specific enthalpy.



The numerical integration of relativistic hydrodynamic equations proceeds on spatially discrete numerical cells in time, based on the finite difference method. In our implementation the state vector  $\mathbf{q}_i^n$  at the cell center  $i$  at the time step  $n$  is updated by calculating the numerical flux vector  $\mathbf{f}_{x,i+1/2}^{n+1/2}$  along the  $x$ -direction at the cell interface  $i + 1/2$  at the half time step  $n + 1/2$  as follows

$$\mathbf{q}_i^{n+1} = \mathbf{q}_i^n - \frac{\Delta t^n}{\Delta x} \left( \mathbf{f}_{x,i+1/2}^{n+1/2} - \mathbf{f}_{x,i-1/2}^{n+1/2} \right). \quad (25)$$

The numerical flux vector is calculated from the approximate Riemann solution and is given in the form

$$\begin{aligned} \mathbf{f}_{x,i+1/2}^{n+1/2} &= \frac{a_{x,i+1/2}^+ \mathbf{F}_x(\mathbf{u}_{L,i+1/2}^{n+1/2}) - a_{x,i+1/2}^- \mathbf{F}_x(\mathbf{u}_{R,i+1/2}^{n+1/2})}{a_{x,i+1/2}^+ - a_{x,i+1/2}^-} \\ &- \frac{a_{x,i+1/2}^+ a_{x,i+1/2}^- \left[ \mathbf{q}(\mathbf{u}_{L,i+1/2}^{n+1/2}) - \mathbf{q}(\mathbf{u}_{R,i+1/2}^{n+1/2}) \right]}{a_{x,i+1/2}^+ - a_{x,i+1/2}^-}, \end{aligned} \quad (26)$$

where the maximum and minimum wave speeds are defined by

$$a_{x,i+1/2}^+ = \max\{0, a_x^+(\mathbf{u}_{L,i+1/2}^{n+1/2}), a_x^+(\mathbf{u}_{R,i+1/2}^{n+1/2})\}, \quad (27)$$

$$a_{x,i+1/2}^- = \min\{0, a_x^-(\mathbf{u}_{L,i+1/2}^{n+1/2}), a_x^-(\mathbf{u}_{R,i+1/2}^{n+1/2})\}. \quad (28)$$

Here  $\mathbf{u}_{L,i+1/2}^{n+1/2}$  and  $\mathbf{u}_{R,i+1/2}^{n+1/2}$  are the left and right state vectors of the primitive variables, which are defined at the left and right edges of the cell interface, respectively. In the first order of spatial accuracy the left and right state vectors reduce to  $\mathbf{u}_{L,i+1/2}^{n+1/2} = \mathbf{u}_i^{n+1/2}$  and  $\mathbf{u}_{R,i+1/2}^{n+1/2} = \mathbf{u}_{i+1}^{n+1/2}$ . For second-order accuracy in space the left and right state vectors are interpolated as

$$\mathbf{u}_{L,i+1/2}^{n+1/2} = \mathbf{u}_i^{n+1/2} + \frac{1}{2} \Delta \mathbf{u}_i^n, \quad \mathbf{u}_{R,i+1/2}^{n+1/2} = \mathbf{u}_{i+1}^{n+1/2} - \frac{1}{2} \Delta \mathbf{u}_{i+1}^n, \quad (29)$$

with the minmod limiter

$$\Delta \mathbf{u}_i^n = \frac{1}{2} \left[ \text{sign}(\Delta^+ \mathbf{u}_i^n) + \text{sign}(\Delta^- \mathbf{u}_i^n) \right] \min\{|\Delta^+ \mathbf{u}_i^n|, |\Delta^- \mathbf{u}_i^n|\}, \quad (30)$$

or the monotonized central limiter

$$\Delta \mathbf{u}_i^n = \frac{1}{2} \left[ \text{sign}(\Delta^+ \mathbf{u}_i^n) + \text{sign}(\Delta^- \mathbf{u}_i^n) \right] \min\{2|\Delta^+ \mathbf{u}_i^n|, 2|\Delta^- \mathbf{u}_i^n|, \frac{1}{2}|\Delta^+ \mathbf{u}_i^n + \Delta^- \mathbf{u}_i^n|\}, \quad (31)$$

where  $\Delta^+ \mathbf{u}_i^n = \mathbf{u}_{i+1}^n - \mathbf{u}_i^n$  and  $\Delta^- \mathbf{u}_i^n = \mathbf{u}_i^n - \mathbf{u}_{i-1}^n$ . In our formulation, the state vector of the primitive variables defined at the half time step,  $\mathbf{u}_i^{n+1/2}$ , is computed from a predictor step,

$\mathbf{q}_i^{n+1/2} = \mathbf{q}_i^n - (\Delta t^n / 2\Delta x)(\mathbf{f}_{x,i+1/2}^n - \mathbf{f}_{x,i-1/2}^n)$ , with the flux vector  $\mathbf{f}_{x,i+1/2}^n$  calculated by replacing the time step  $n + 1/2$  by the time step  $n$  in equations (26) to (29). This approach makes our code second order in time as well.

The time step is restricted by the Courant condition  $\Delta t^n = C_{\text{cour}}\Delta x / \max\{|a_{x,i+1/2}^\pm|\}$  with  $C_{\text{cour}} < 1$ . For multidimensional extensions, the numerical integration along the  $x$ -direction is applied separately to the  $y$ - (and  $z$ -) directions through the Strang-type dimensional splitting (Strang 1968). In order to maintain second-order accuracy the order of dimensional splitting is completely permuted in each successive sequence.

## 4. Test Problems

We have applied the numerical scheme with the general equation of state, described in previous sections, to several test problems. In all the test problems the minmod limiter and a Courant constant,  $C_{\text{cour}} = 0.4$ , are used.

### 4.1. Relativistic Shock Tube

The relativistic shock tube test is characterized initially by two different states separated by a discontinuity. As the initial discontinuity decays, distinct wave patterns consisting of shock waves, contact discontinuities, and rarefaction waves appear in the subsequent flow evolution. In the relativistic shock tube problem the decay of the initial discontinuity significantly depends on the tangential velocity since the velocity components are coupled through the Lorentz factor in the equations and the specific enthalpy also couples with the tangential velocity (Pons et al. 2000). As a result, the relativistic shock tube problem becomes more challenging in the presence of tangential velocities. This relativistic shock tube problem is very good test since it has an analytic solution (Pons et al. 2000; Giacomazzo & Rezzolla 2006) where the numerical solution can be compared.

We have performed two sets of the two-dimensional relativistic shock tube tests using the general equation of state for an electron-positron gas. The first test set is less relativistic, with  $h \sim 5$ , while the second test set is more severe, with a large initial internal energy ( $h \gg 1$ ). For each of the test sets, two cases are presented, one having only parallel velocity components while the other has, in addition, tangential velocities. In the first set, the initial left and right states for the case of only parallel velocities are given by  $\rho_L = 10$ ,  $\rho_R = 1$ ,  $v_{p,L} = 0$ ,  $v_{p,R} = 0$ ,  $p_L = 13.3$ , and  $p_R = 10^{-6}$ ; for the case where tangential velocities are included these additional initial values are  $v_{t,L} = 0.9$  and  $v_{t,R} = 0.9$ . For the second set

the initial left and right states for the case of only parallel velocity are  $\rho_L = 1$ ,  $\rho_R = 1$ ,  $v_{p,L} = 0$ ,  $v_{p,R} = 0$ ,  $p_L = 10^3$ , and  $p_R = 10^{-2}$ ; now for the case when tangential velocities are considered as well,  $v_{t,L} = 0.99$  and  $v_{t,R} = 0.99$  are taken. Here the subscripts  $L$  and  $R$  denote the left and right states separated by an initial discontinuity placed along the main diagonal in the two-dimensional computational plane. Structures such as waves and discontinuities propagate along the diagonal normal to the initial discontinuity. Here  $v_p$  is velocity parallel to the wave normal in the plane, given by  $v_p = \sqrt{v_x^2 + v_y^2}$  and  $v_t$  is velocity tangential to the wave normal in the direction out of the plane, given by  $v_t = v_z$ . The numerical computations are performed in a two-dimensional box with  $x = [0, 1]$  and  $y = [0, 1]$  using  $512 \times 512$  cells for the first set and  $2048 \times 2048$  cells for the second set.

The results from the numerical computations carried with the general equation of state for an electron-positron gas for the first test set are shown in Figure 3. Wave structures are measured along the main diagonal line  $x = y = 0$  to 1 at times  $t = 0.4\sqrt{2}$  and  $0.8\sqrt{2}$  for the cases of the only parallel and also tangential velocities, respectively. The numerical solutions are marked with open circles and the analytical solutions obtained using the numerical code available from Giacomazzo & Rezzolla (2006) are plotted with solid lines. Our numerical scheme with the proposed general equation of state is able to reproduce all the wave structures with very good accuracy and stability, as shown in Figure 3. The shock waves and rarefaction waves are captured correctly, while the contact discontinuities are relatively more smeared due to the use of the HLL scheme and the minmod limiter. The inclusion of the tangential velocity leads to the same basic wave pattern as in the absence of tangential velocity, but the numerical solutions are significantly modified.

Figure 4 shows the results from the numerical computations with the general equation of state for an electron-positron gas for the second test set. Structures are measured along the main diagonal line  $x = y = 0$  to 1 at times  $t = 0.4\sqrt{2}$  and  $1.8\sqrt{2}$  for the cases of the parallel only and included tangential velocities, respectively. The numerical solutions compare well with the analytical solutions. Shock waves and contact discontinuities propagate to the right, while rarefaction waves move to the left. As shown in Figure 4, all the wave structures are accurately reproduced and their stability is good; however, the contact discontinuities are somewhat smeared. Again, the inclusion of the tangential velocity has a considerable influence on the numerical solutions.

For a quantitative comparison with analytical solutions we have calculated the norm errors of the rest mass density, parallel and tangential velocities, and pressure defined by, e.g., for density,  $\|E(\rho)\| = \sum_{i,j} |\rho_{i,j}^N - \rho_{i,j}^A| \Delta x_i \Delta y_j$ , where the superscripts  $N$  and  $A$  represent numerical and analytical solution, respectively. The norm errors are given in Table 1 and demonstrate a very good agreement between the numerical and analytical solutions in all

the primitive variables. We also carried out the two-dimensional relativistic shock tube tests considered in Figures 3 and 4 for several other possible combinations of the tangential velocity pairs  $v_{t,L} = 0, 0.9, 0.99$  and  $v_{t,R} = 0, 0.9, 0.99$ . In general, the stable wave structures are reproduced and the numerical solutions are reasonably comparable to the analytical solutions for all the different combinations of tangential velocity pairs. As a consequence, the results from the two-dimensional relativistic shock tube tests show that our code is able to robustly and accurately capture discontinuities and waves.

## 4.2. Relativistic Shock Reflection

The relativistic shock reflection problem involves a collision between two equal gas flows moving at relativistic speeds in opposite directions. The collision of the two cold gases causes compression and heating of the gases as kinetic energy is converted into internal energy. This generates the two strong shock waves to propagate in opposite directions, leaving the gas behind the shocks stationary. The analytical solution of this relativistic shock reflection problem is obtained by Blandford & McKee (1976) and Giacomazzo & Rezzolla (2006).

We have tested the two-dimensional relativistic shock reflection problem using the general equation of state for an electron-positron gas. Two cases are presented here. As for the shock tube tests, one includes only the parallel velocity and the other includes in addition the tangential velocity. The left and right states for the case of only parallel velocity are initially given by  $\rho_L = 1$ ,  $\rho_R = 1$ ,  $v_{p,L} = 0.99$ ,  $v_{p,R} = -0.99$ ,  $p_L = 10^{-6}$ , and  $p_R = 10^{-6}$ , and for the case when the tangential velocity is included, oppositely directed tangential velocities  $v_{t,L} = 0.1$  and  $v_{t,R} = -0.1$  are assumed to be present on either side of the plane. Here the subscripts  $L$  and  $R$  stand for the left and right states separated by the initial collision points located along the main diagonal in the two-dimensional computational plane. The two shock waves propagate diagonally in opposite directions, and should keep symmetric with respect to the initial collision points. As in the relativistic shock tube tests,  $v_p$  is velocity parallel to the wave normal in the plane and  $v_t$  is velocity tangential to the wave normal in the direction out of the plane. The numerical computations are carried out in a two-dimensional box with  $x = [0, 1]$  and  $y = [0, 1]$  using  $512 \times 512$  cells.

Figure 5 shows the results from our relativistic shock reflection tests with the general equation of state for an electron-positron gas. Structures are measured along the main diagonal line  $x = y = 0$  to  $1$  at time  $t = 0.8\sqrt{2}$ . The numerical solutions are in very good agreement with the analytical solutions. In both cases, the shock wave is resolved by two numerical cells, and there are no numerical oscillations behind the shocks. As shown in Figure 5, the compression ratio between shocked and unshocked gases is about 30 for

the rest mass density and about 70 for the pressure in the case of only parallel velocities; the inclusion of the tangential velocities increases the compression ratio to about 40 for the rest mass density and to about 140 for the pressure. Near  $x = y = 0.5$ , the density distribution slightly underestimates the analytical solution and a stationary discontinuity in the tangential velocity is somewhat diffused due to the numerical effect of reflection heating phenomena. The norm errors of the rest mass density, parallel and tangential velocities, and pressure are also given in Table 1. A direct comparison with the analytical solutions shows that the measured errors are very small for all the primitive variables.

The accuracy of numerical solutions depends on the number of cells spanned by the computational box. We have run the relativistic shock reflection test in Figure 5(b) with different numerical resolutions to check the convergence rate. Except for the numerical resolutions the initial conditions are identical to those used in the test in Figure 5(b). We have computed the norm errors for rest mass density, velocities, and pressure with different resolutions. Numerical resolutions of  $16^2$ ,  $32^2$ ,  $64^2$ ,  $128^2$ ,  $256^2$ , and  $512^2$  cells give norm errors for the rest mass density of 7.56, 4.74, 2.38, 1.17, 0.48, and 0.25, respectively. As expected for discontinuous problems, first-order convergence in the norm errors for rest mass density is obtained with increasing the numerical resolution. Similar clear trends toward convergence are seen in the norm errors for velocities and pressure.

### 4.3. Relativistic Blast Wave

In a relativistic blast wave test a large amount of energy is initially deposited in a small finite spherical volume and the subsequent expansion of that overpressured region is evolved forward in time. This produces a spherical shock propagating outward from an initial discontinuity at an arbitrary radius. This radial blast wave explosion provides a useful test problem to explore the spherically symmetric properties in highly relativistic flow speeds.

We have performed the three-dimensional relativistic blast wave test with the general equation of state for an electron-proton gas. The initial condition for the relativistic blast wave problem consists of two constant states given by  $\rho_I = 1$ ,  $\rho_O = 1$ ,  $v_I = 0$ ,  $v_O = 0$ ,  $p_I = 10^3$ , and  $p_O = 1$ , where subscripts  $I$  and  $O$  represent the inner and outer states separated by an initial discontinuity at the radius  $r = 0.5$  in the three-dimensional computational box. The numerical computations are performed in a three-dimensional box with  $x = [0, 1]$ ,  $y = [0, 1]$ , and  $z = [0, 1]$  using  $256 \times 256 \times 256$  cells. Outflow boundary conditions are used at all boundaries except at the symmetry axis where reflecting boundary conditions are imposed.

Figure 6 shows the profiles of rest mass density, radial velocity, and pressure along the radial distance in the relativistic blast wave tests. Radial structures are measured along the main diagonal line  $x = y = z = 0$  to 1 at time  $t = 0.4$ . Numerical computations carried out with our general equation of state for an electron-proton gas, as well as with the ideal gas equation of state with constant adiabatic index  $\gamma = 5/3$  are shown. In both cases, high Lorentz factors (up to  $\sim 15$ ) are generated and the radial symmetry is well preserved. However, compared to the  $\gamma = 5/3$  case, the results obtained with the electron-proton case show significant differences. In fact, the spherical shock wave has a higher density peak and propagates at a slower radial velocity in the electron-proton case.

In Figure 7, we present the images of rest mass density, pressure, and Lorentz factor in the relativistic blast wave test with the general equation of state for an electron-proton gas. The images are shown in logarithmic scales on the plane  $x = 0$  at time  $t = 0.4$ . As shown in the images, the spherical shock wave propagates to larger radius very well, preserving the initial spherical symmetry.

## 5. Relativistic Axisymmetric Jets

As a practical astrophysical problem using this code, we consider the propagation of relativistic axisymmetric jets in three dimensions. The simulation of a relativistic jet has been presented as a test simulation in almost all relativistic hydrodynamic codes, using the ideal gas equation of state with a constant adiabatic index (e.g., Aloy et al. 1999; Del Zanna & Bucciantini 2002; Mignone & Bodo 2005). We have performed this relativistic jet simulation to confirm the accuracy and robustness of our numerical scheme incorporating the proposed general equation of state as well as to make a preliminary investigation of the influence of the equation of state on the propagation of relativistic jets.

Some previous investigations of relativistic jet propagation have concentrated on the importance of a realistic equation of state in relativistic jet flows. Mignone & McKinney (2007) addressed the effect of a realistic equation of state on relativistic (magnetized) flows including relativistic jets. They showed that the choice of a realistic equation of state can significantly alter the solution when large temperature gradients are present. To study the evolution of low-power jets Perucho & Martí (2007) performed numerical simulations using an equation of state for a two-component relativistic gas that separately treats leptonic and baryonic matter. Rossi et al. (2008) examined the dynamical evolution of relativistic light jets in the presence of an induced perturbation using a Synge-like equation of state for a single-component relativistic gas.

The approximate propagation velocity of the jet through the homogeneous ambient medium can be derived from momentum flux balance between the beam and ambient medium in the reference frame of the working surface that separates beam and shocked ambient gas (e.g., Martí et al. 1997). Assuming pressure equilibrium between the beam and the ambient medium, the one-dimensional jet advance velocity, estimated in the rest frame of the ambient medium, is then

$$v_a = \frac{\Gamma_b \sqrt{\eta h_b / h_a}}{1 + \Gamma_b \sqrt{\eta h_b / h_a}} v_b, \quad (32)$$

where  $\eta$  and  $\Gamma_b$  are given by  $\eta = \rho_b / \rho_a$  and  $\Gamma_b = 1 / \sqrt{1 - v_b^2}$ . Here the subscripts  $b$  and  $a$  indicate the beam and the ambient medium, respectively. The morphology and dynamics of the relativistic jet propagating into the homogeneous medium is commonly specified by the beam to ambient medium density ratio  $\eta$ , the beam Lorentz factor  $\Gamma_b$ , and the beam Mach number  $M_b = v_b / c_{s,b}$ .

We have considered the three-dimensional simulations of relativistic jets using different equations of state. Table 2 lists the simulation parameters of the four different cases corresponding to the ideal gas equation of state with constant adiabatic index  $\gamma = 5/3$  and  $4/3$  and the proposed general equation of state for electron-positron and electron-proton gases. In all these cases, we choose the beam density  $\rho_b = 0.1$ , the ambient medium density  $\rho_a = 10$ , the beam velocity  $v_b = 0.99$  and we assume that the beam is in pressure equilibrium with the ambient medium,  $p_b = p_a$ . This gives the density contrast  $\eta = 10^{-2}$ , the beam Lorentz factor  $\Gamma_b = 7.1$ , and the beam Mach number  $M_b = 2$ . The numerical simulations have been performed in the three-dimensional computational box with  $x = [0, 1]$ ,  $y = [0, 1]$ , and  $z = [0, 4]$  using a uniform numerical grid of  $128 \times 128 \times 512$  cells. The beam has an initial radius  $r_b = 1/8$  (corresponding to 16 cells), is launched from the origin, and propagates through a uniform static ambient medium along the positive  $z$ -direction. Outflow boundary conditions are set at all boundaries except along the symmetry axis where reflecting boundary conditions are used and in the injection region where an inflow boundary condition is imposed to keep the beam constantly fed. The monotonized central limiter and the Courant constant  $C_{\text{cour}} = 0.2$  are used in all these jet propagation cases.

The images in Figure 8 display the logarithms of the rest mass density on the plane  $x = 0$  at time  $t = 6$  for the four different cases in the simulations of relativistic axisymmetric jets. The bow shock, the beam, and the cocoon surrounding the beam can be clearly identified in all four cases, confirming the ability of our code to follow complex relativistic flows. For each case, a bow shock that separates the shocked jet material from the shocked ambient medium is driven into the ambient medium. The beam itself is terminated by a Mach disk where much of the beam’s kinetic energy is converted into internal energy. Shocked jet material flows backward along the working surface into a cocoon, resulting in the development and

mixture of turbulent vortices in the cocoon, and the interaction of these vortices with the beam forms oblique internal shocks within the beam close to the Mach disk, which causes the deceleration of the jet. The four different cases, however, show differences in specific morphological and dynamical properties. The cold jet (case A) propagates at the slowest velocity, and the jet produces a broad bow shock, a thick cocoon, and has the Mach disk located quite far behind the bow shock. On the contrary, the hot jet (case B) is dominated by a narrow bow shock, has a thin cocoon, and its Mach disk lies very close to the bow shock, thanks to its having the fastest advance velocity. The electron-positron and the electron-proton jets (cases C and D) propagate faster than the cold jet, but slower than the hot jet. Therefore, the electron-positron and the electron-proton jets possess morphological and dynamical properties intermediate between the cold and the hot jets. In terms of our simulation parameters, the electron-positron jet tends to be more similar to the cold jet, while the electron-proton jet seems to share more features with the hot jet.

In Figure 9, the position of the bow shock is plotted as a function of time for the four different gases. The symbols mark the numerical estimate for a selected time interval for each case, and the lines represent the one-dimensional theoretical estimate in equation (32). The numerical simulations are in good agreement with the one-dimensional theoretical estimates for the bow shock location for all cases.

## 6. Conclusion

Most numerical codes for special relativistic hydrodynamics have used the ideal gas equation of state with a constant adiabatic index, but this is a poor approximation for most relativistic astrophysical flows. We proposed a new general equation of state for a multi-component relativistic gas, based on the Synge equation of state for a relativistic perfect gas (Synge 1957). Our proposed general equation of state is very efficient and suitable for numerical relativistic hydrodynamics since it has an analytic expression. The thermodynamic quantities computed using the proposed general equation of state behave correctly asymptotically in the limits of hot and cold gases. For intermediate regimes the thermodynamic quantities vary between those for the two limiting cases, depending on the composition of the relativistic gas.

We also presented a multidimensional relativistic hydrodynamics code incorporating the proposed general equation of state for a multi-component relativistic gas. Our numerical code is based on the HLL scheme (Harten et al. 1983), which avoids a full characteristic decomposition of the relativistic hydrodynamic equations and uses an approximate solution to the Riemann problem for flux calculations. Since the numerical code is fully explicit, re-



taining a second-order accuracy in space and time, it is simple to extend the code to different geometries or to produce parallelized versions of this code. The analytical formulation of the proposed equation of state and the numerical scheme being free of complete characteristic decomposition make the code very efficient and robust in ultrarelativistic multidimensional problems.

The accuracy and robustness of the code are demonstrated in two dimensions using the test problems of the relativistic shock tube and the relativistic shock reflection and in three dimensions using the test problem of the relativistic blast wave. The direct comparisons of numerical results with analytical solutions show that shocks and discontinuities are correctly resolved even in highly relativistic test problems with nonvanishing tangential velocities. Results from the three-dimensional simulations of the relativistic axisymmetric jets demonstrate the ability of our code to follow complex relativistic flows as well as the flexibility enough to be applied to practical astrophysical problems. These simulations show that the morphology and dynamics of the relativistic jets are significantly influenced by the different equation of state and by different compositions of a relativistic perfect gas.

This work was supported by the National Research Foundation of Korea Grant funded by the Korean Government (NRF-2009-351-C00029).

## REFERENCES

- Aloy, M. A., Ibáñez, J. M., Martí, J. M., & Müller, E. 1999, *ApJS*, 122, 151
- Anninos, P., & Fragile, P. C. 2003, *ApJS*, 144, 243
- Blandford, R. D., & McKee, C. F. 1976, *Phys. Fluids*, 19, 1130
- Choi, E., Wiita, P. J., & Ryu, D. 2007, *ApJ*, 655, 769
- Del Zanna, L., & Bucciantini, N. 2002, *A&A*, 390, 1177
- Donat, R., Font, J. A., Ibáñez, J. M., & Marquina, A. 1998, *J. Comput. Phys.*, 146, 58
- Duncan, G. C., & Hughes, P. A. 1994, *ApJ*, 436, L119
- Einfeldt, B. 1988, *SIAM J. Numer. Anal.*, 25, 294
- Falle, S. A. E. G., & Komissarov, S. S. 1996, *MNRAS*, 278, 586
- Giacomazzo, B., & Rezzolla, L. 2006, *J. Fluid Mech.*, 562, 223

- Harten, A., Lax, P. D., & van Leer, B. 1983, *SIAM Rev.*, 25, 35
- Hughes, P. A., Miller, M. A., & Duncan, G. C. 2002, *ApJ*, 572, 713
- Komissarov, S. S., & Falle, S. A. E. G. 1998, *MNRAS*, 297, 1087
- Landau, L. D., & Lifshitz, E. M. 1959, *Fluid Mechanics* (London: Pergamon Press)
- Lister, M. L., et al. 2009, *AJ*, 138, 1874
- Martí, J. M., Müller, E., Font, J. A., Ibáñez, J. M., & Marquina, A. 1997, *ApJ*, 479, 151
- Mathews, W. G. 1971, *ApJ*, 165, 147
- Meliani, Z., Keppens, R., & Giacomazzo, B. 2008, *A&A*, 491, 321
- Meliani, Z., Sauty, C., Tsinganos, K., & Vlahakis, N. 2004, *A&A*, 425, 773
- Mignone, A., & Bodo, G. 2005, *MNRAS*, 364, 126
- Mignone, A., & McKinney, J. C. 2007, *MNRAS*, 378, 1118
- Mignone, A., Plewa, T., & Bodo, G. 2005, *ApJS*, 160, 199
- Norman, M. L., Winkler, K.-H. A., Smarr, L., & Smith, M. D. 1982, *A&A*, 113, 285
- Perucho, M., & Martí, J. M. 2007, *MNRAS*, 382, 526
- Pons, J. A., Martí, J. M., & Müller, E. 2000, *J. Fluid Mech.*, 422, 125
- Rosen, A., Hughes, P. A., Duncan, G. C., & Hardee, P. E. 1999, *ApJ*, 516, 729
- Rossi, P., Mignone, A., Bodo, G., Massaglia, S., & Ferrari, A. 2008, *A&A*, 488, 795
- Scheck, L., Aloy, M. A., Martí, J. M., Gómez, J. L., & Müller, E. 2002, *MNRAS*, 331, 615
- Schneider, V., Katscher, U., Rischke, D. H., Waldhauser, B., Maruhn, J. A., & Munz, C.-D. 1993, *J. Comput. Phys.*, 105, 92
- Strang, G. 1968, *SIAM J. Numer. Anal.*, 5, 506
- Synge, J. L. 1957, *The Relativistic Gas* (Amsterdam: North-Holland)
- Wilson, J. R., & Mathews, G. J. 2003, *Relativistic Numerical Hydrodynamics* (Cambridge: Cambridge Univ. Press)

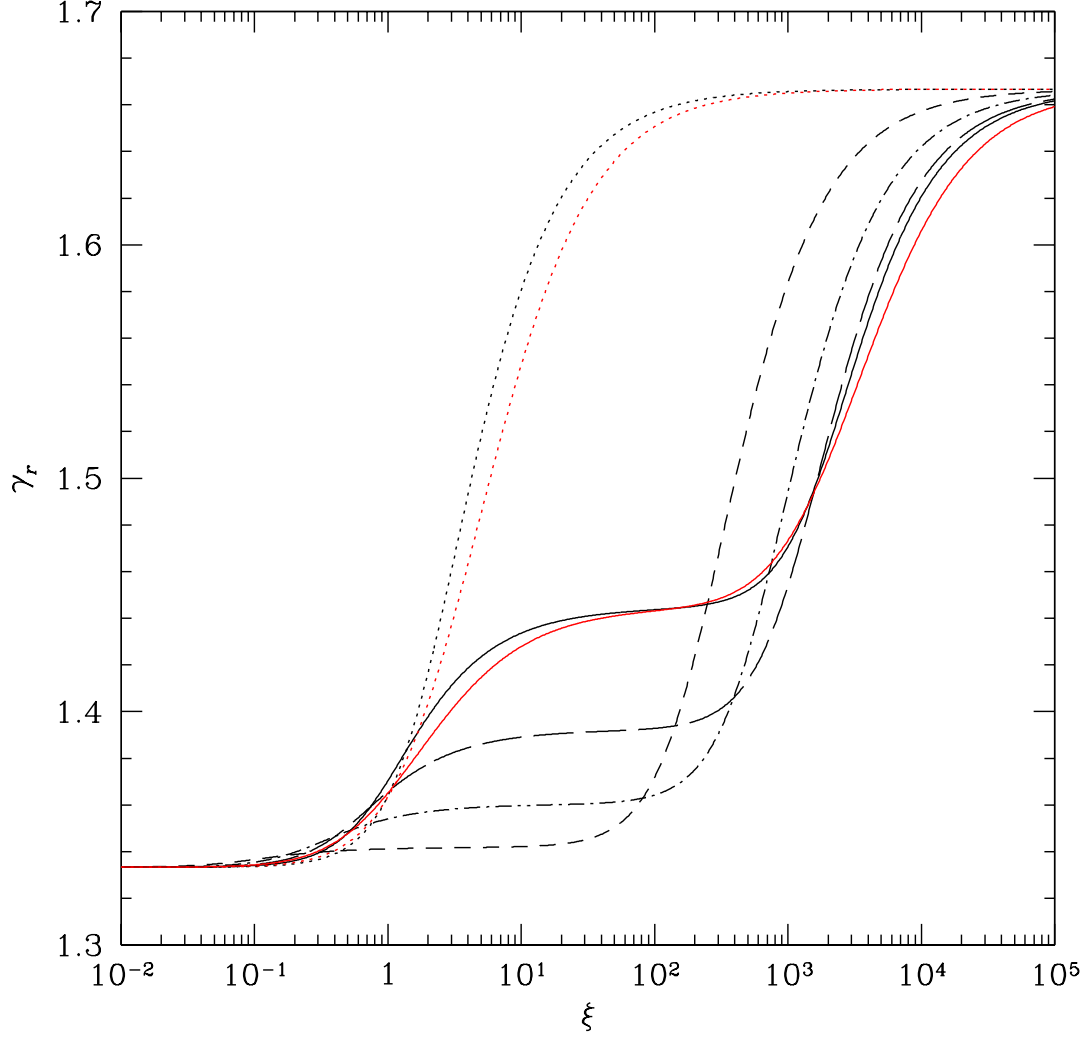


Fig. 1.— The relativistic adiabatic index,  $\gamma_r$ , as function of inverse temperature,  $\xi$ , for different compositions of relativistic gas. The compositions of  $\chi = 0$  (electron-positron), 0.1, 0.3, 0.6, and 1 (electron-proton) are shown using dotted, short dashed, dot-short dashed, long dashed, and solid curves, respectively. The exact Synge solutions for electron-positron and electron-proton gases are respectively drawn as the red dotted and solid lines for comparison.

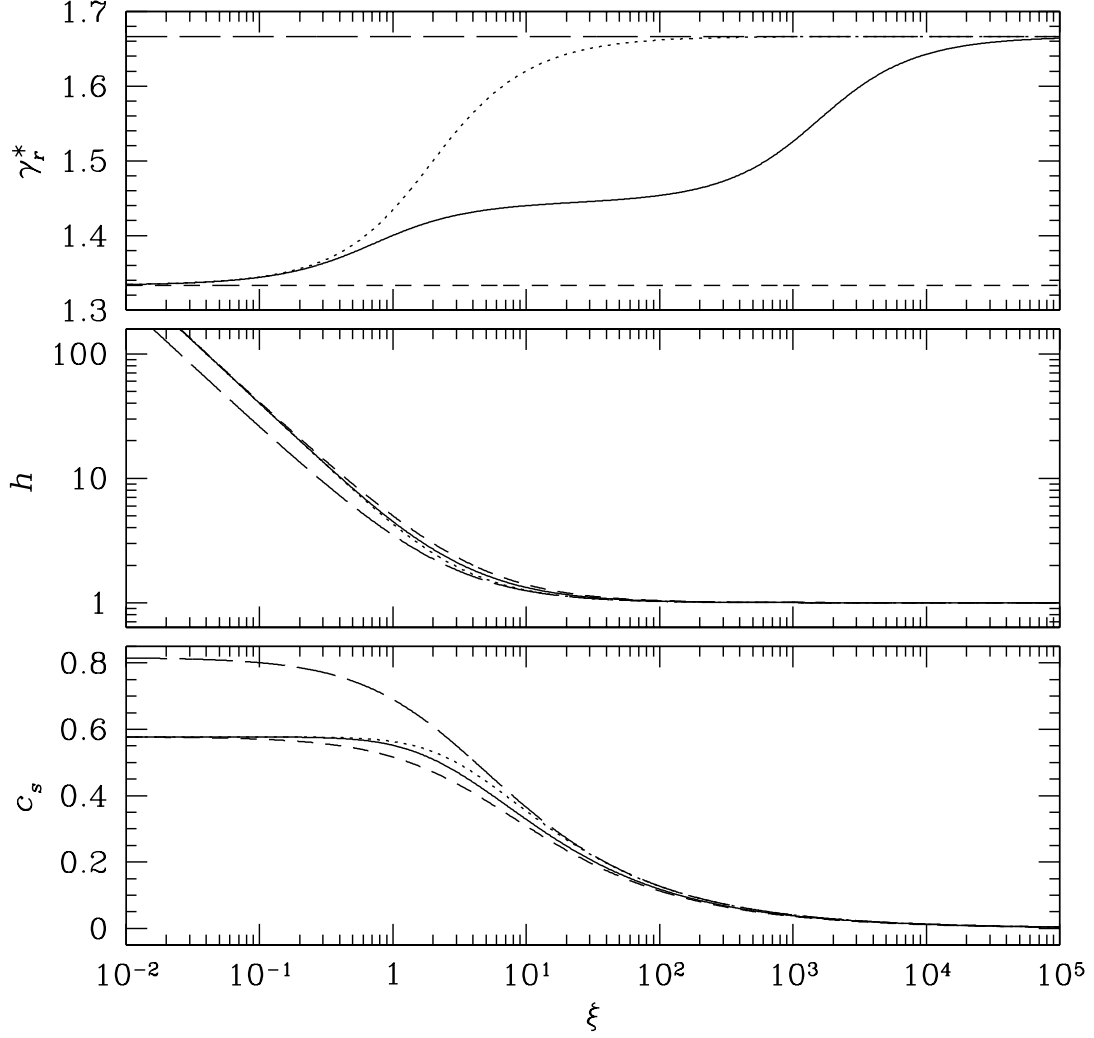


Fig. 2.— The quantity  $\gamma_r^*$ , specific enthalpy  $h$ , and sound speed  $c_s$ , as functions of inverse temperature  $\xi$  for the different equation of state. The long dashed and short dashed lines correspond to the ideal gas equation of state with constant adiabatic index  $\gamma = 5/3$  and  $4/3$ , respectively. Results for the proposed general equation of state for electron-positron and electron-proton gases are shown by the dotted and solid lines, respectively.

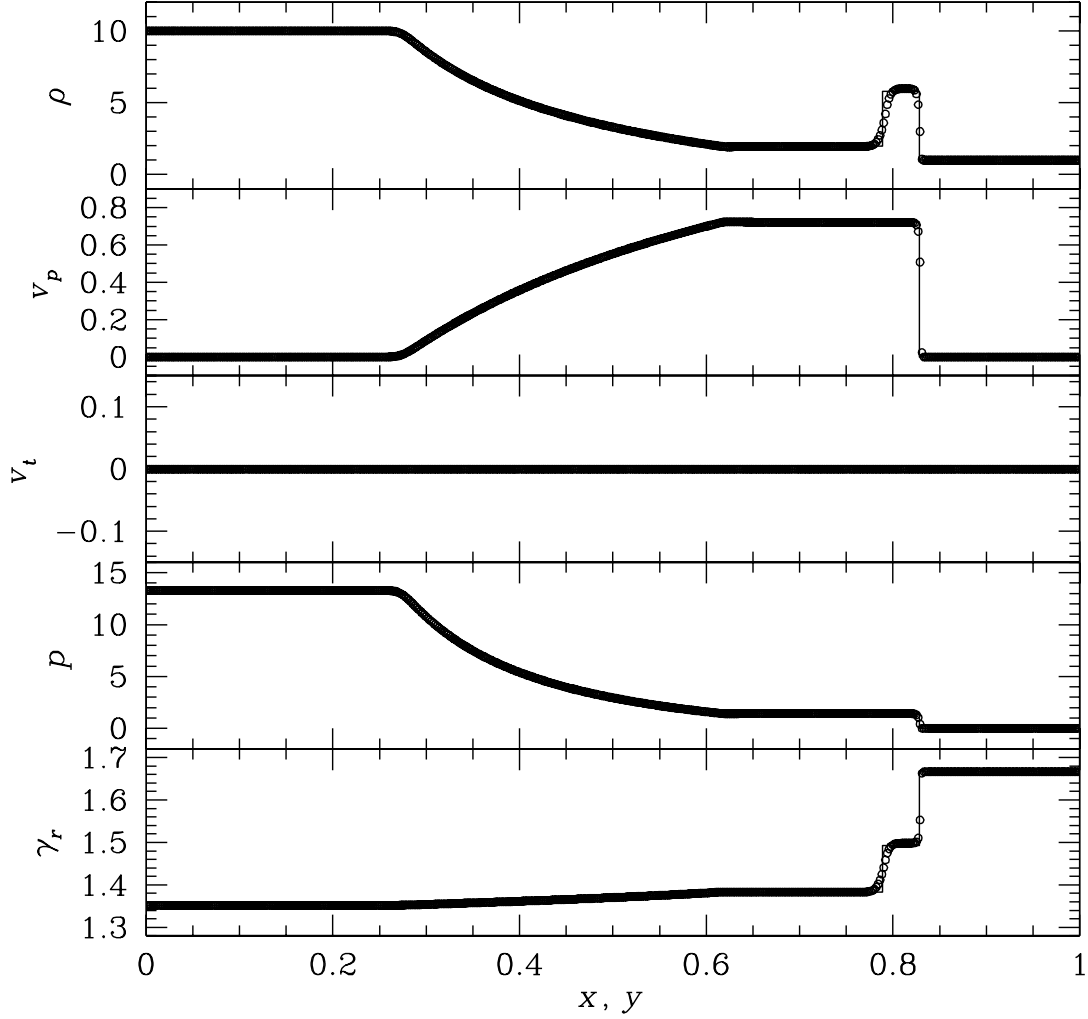
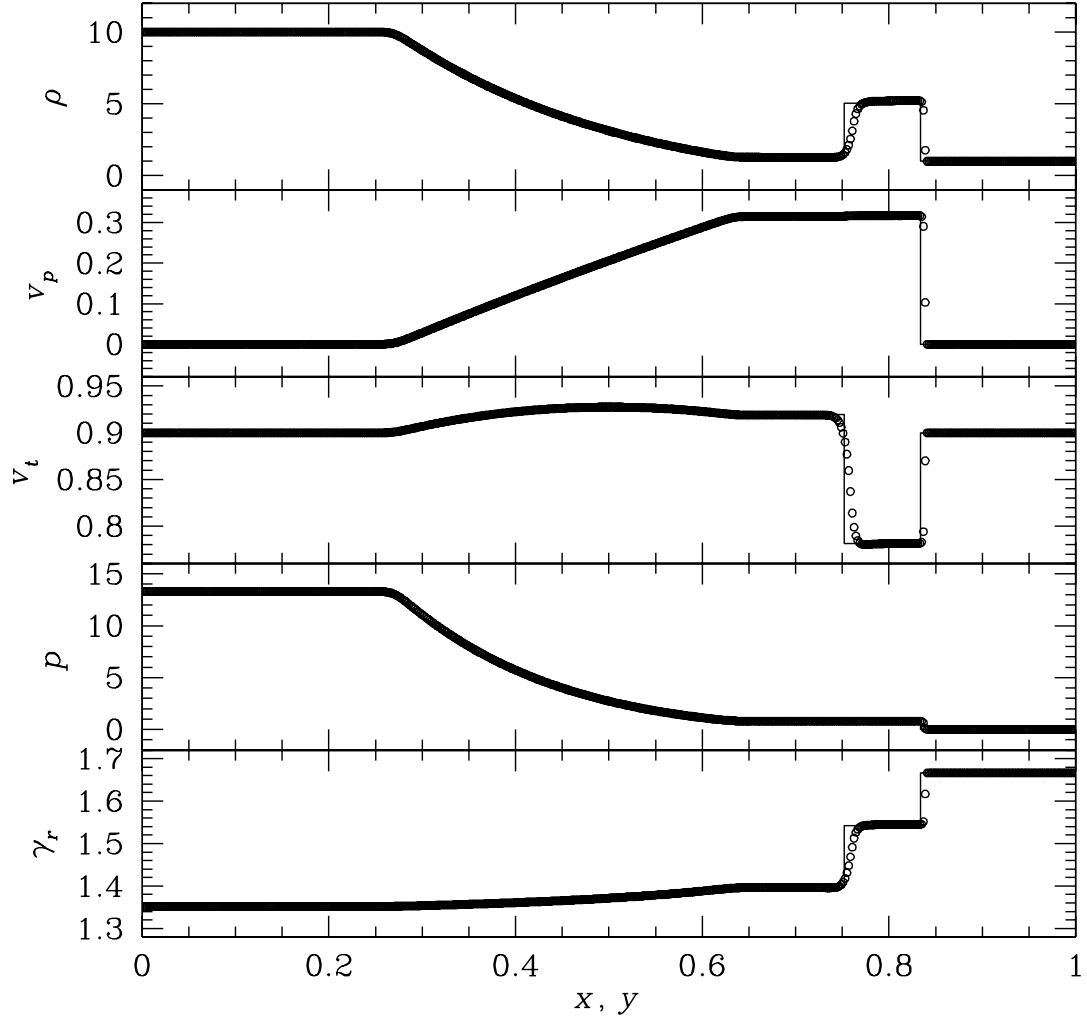


Fig. 3.— (a) The two-dimensional relativistic shock tube test with the general equation of state for an electron-positron gas for the case of the parallel velocity in the first (moderately relativistic) test set. The numerical computation is performed in a square box with  $x = y = [0, 1]$  using  $512^2$  cells, and the wave structures are measured along the main diagonal line  $x = y = 0$  to  $1$  at time  $t = 0.4\sqrt{2}$ . The numerical solutions are marked with open circles and the analytical solutions are plotted with solid lines. (b) Same as in (a) but for the case of the included tangential velocity and at time  $t = 0.8\sqrt{2}$ .



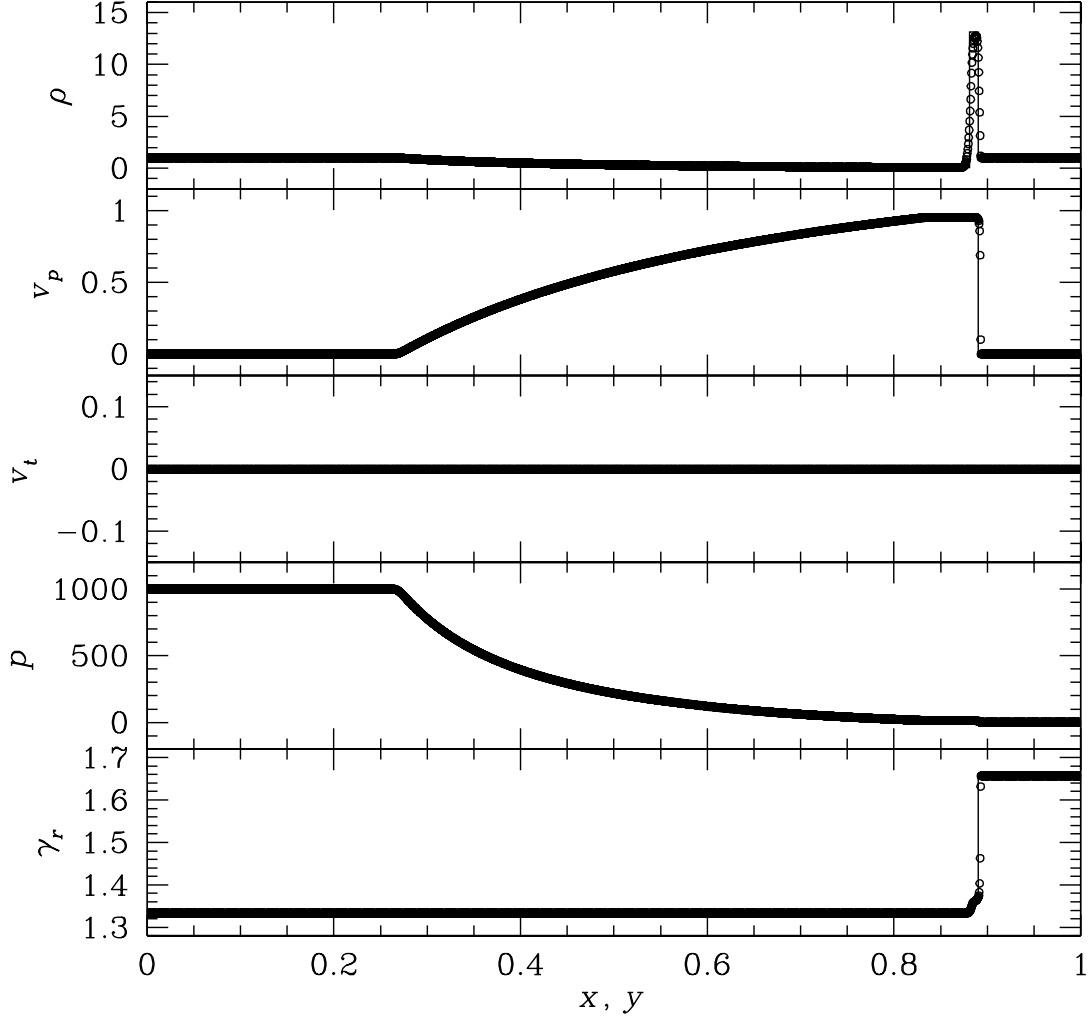
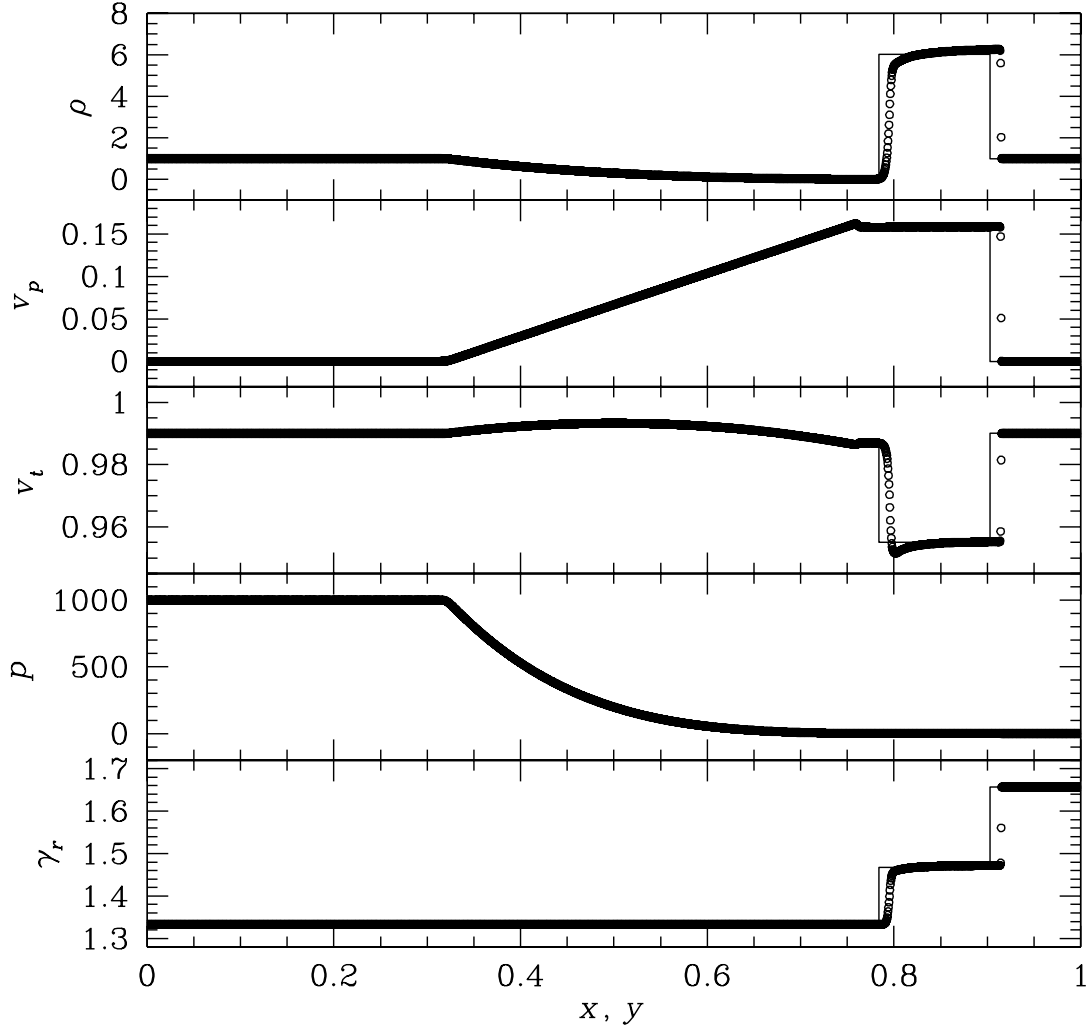


Fig. 4.— (a) The two-dimensional relativistic shock tube test with the general equation of state for an electron-positron gas for the case of the parallel velocity in the second (highly relativistic) test set. The numerical computation is performed in a square box with  $x = y = [0, 1]$  using  $2048^2$  cells, and the wave structures are measured along the main diagonal line  $x = y = 0$  to  $1$  at time  $t = 0.4\sqrt{2}$ . The numerical solutions are marked with open circles and the analytical solutions are plotted with solid lines. (b) Same as in (a) but for the case of the included tangential velocity and at time  $t = 1.8\sqrt{2}$ .





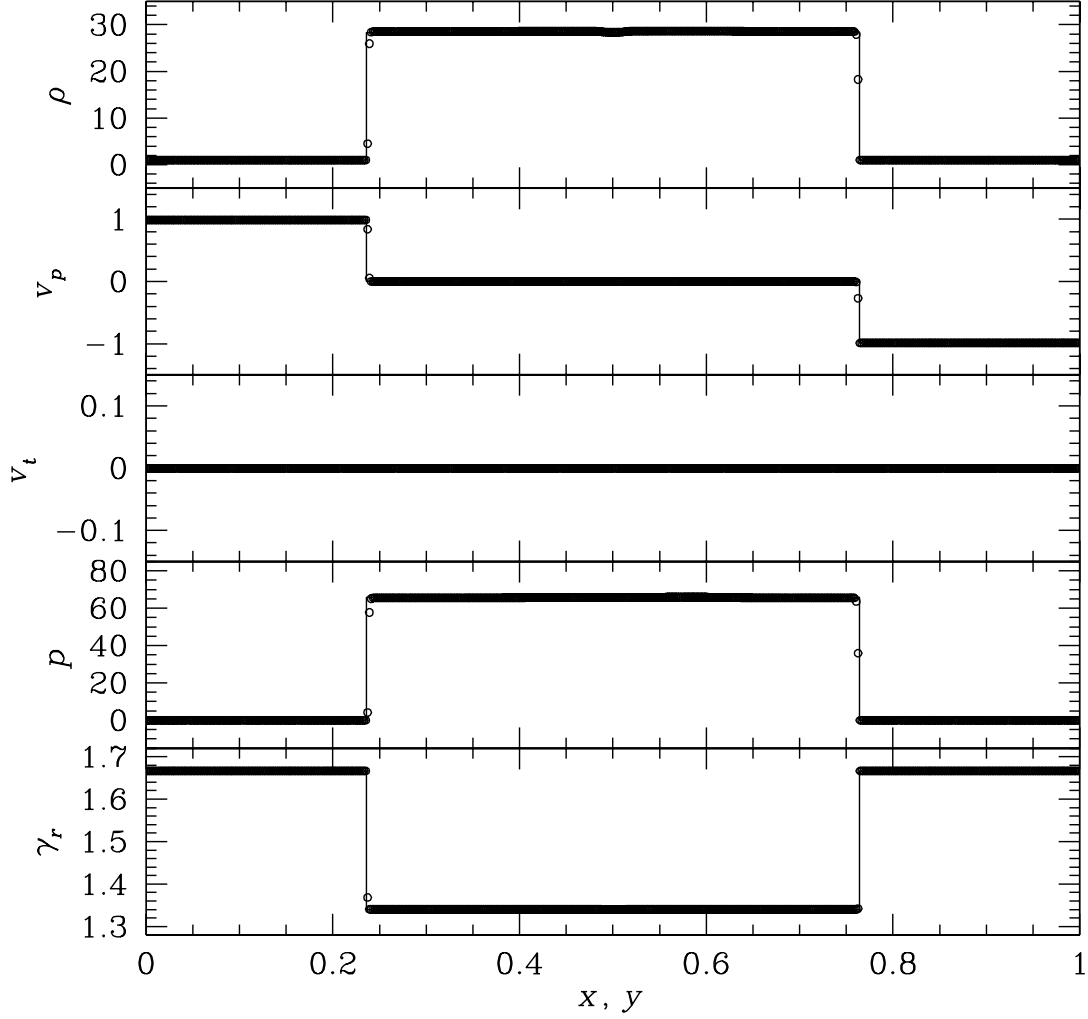
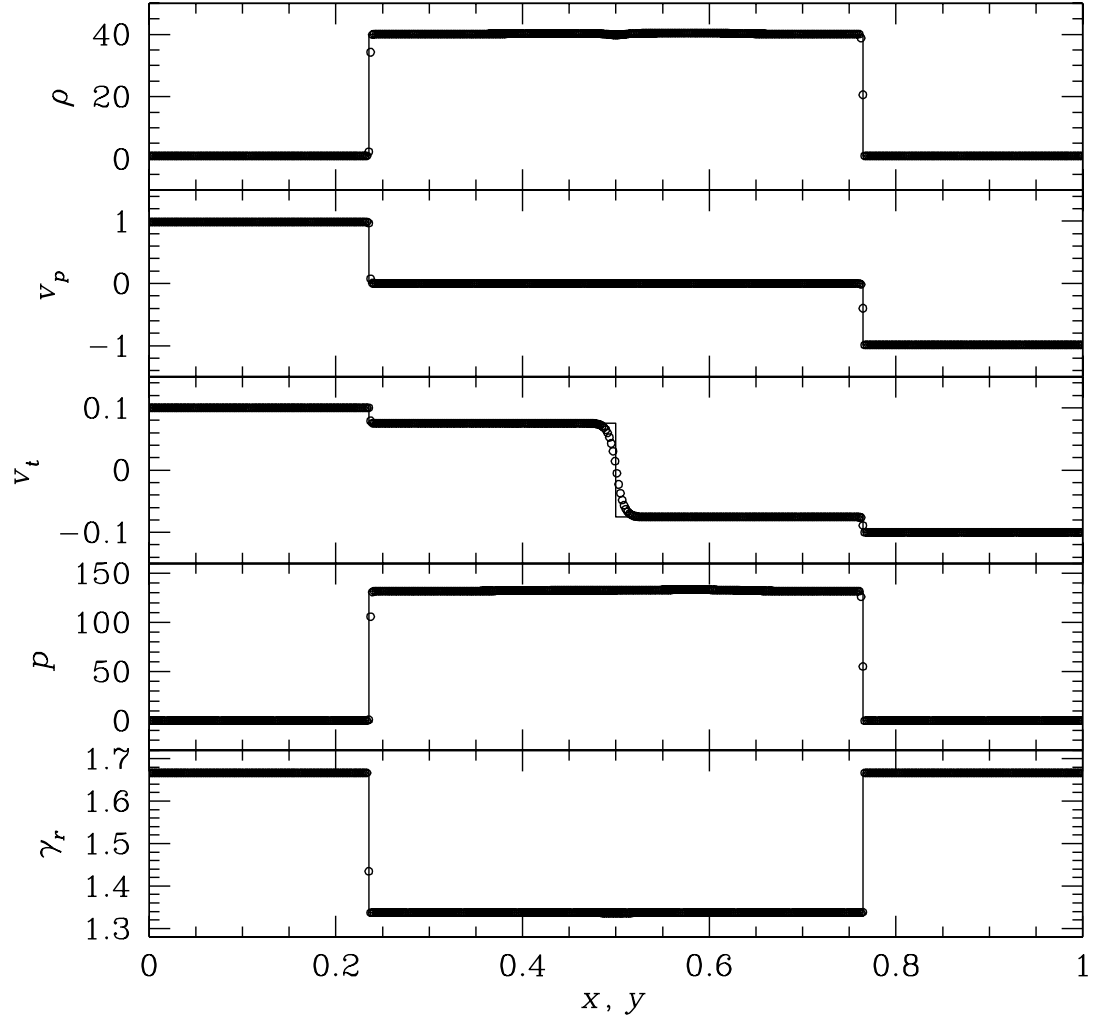


Fig. 5.— (a) The two-dimensional relativistic shock reflection tests with the general equation of state for an electron-positron gas for the case of the parallel velocity. The numerical computations are performed in a square box with  $x = y = [0, 1]$  using  $512^2$  cells, and structures are measured along the main diagonal line  $x = y = 0$  to  $1$  at time  $t = 0.8\sqrt{2}$ . The numerical solutions are marked with open circles and analytical solutions are plotted with solid lines. (b) Same as in (a) but for the case of the included tangential velocity.



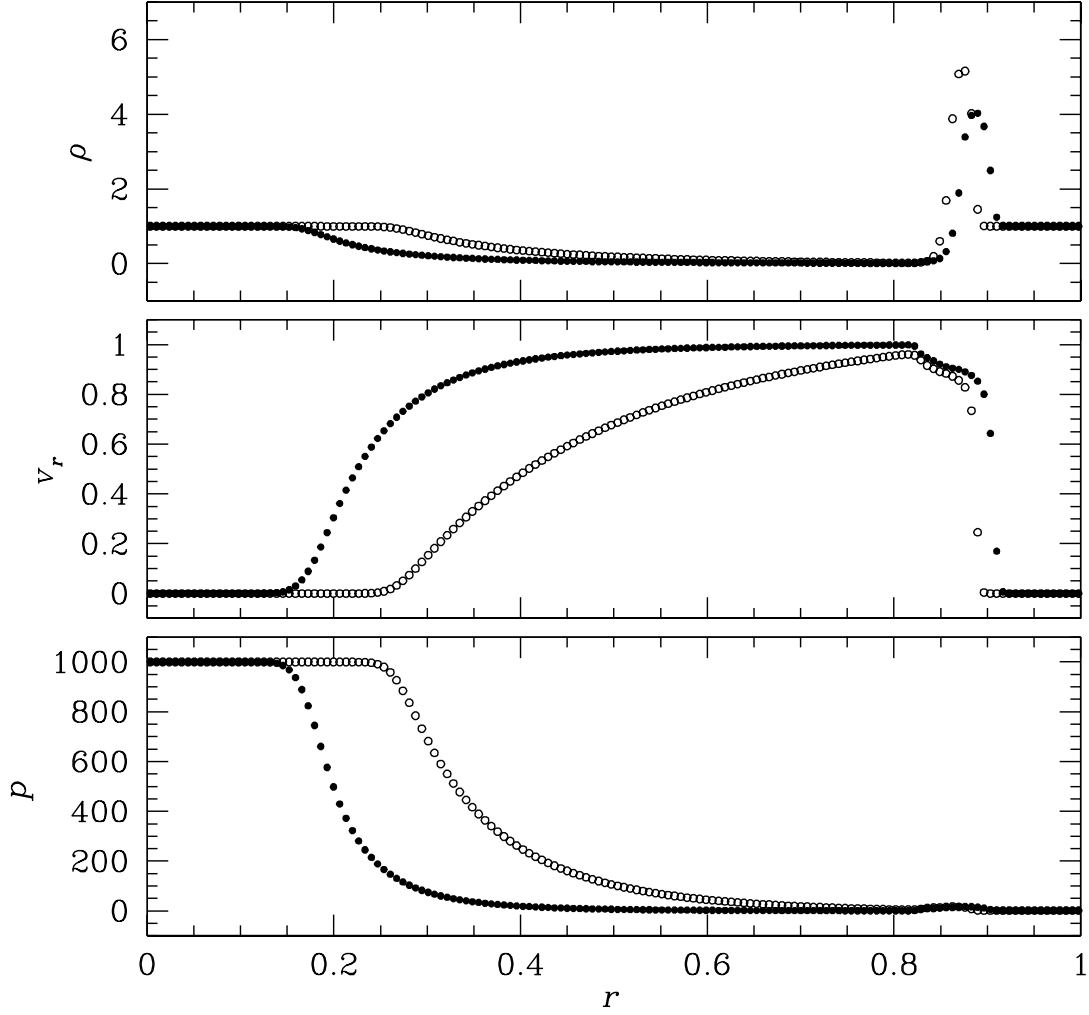


Fig. 6.— Profiles of rest mass density  $\rho$ , radial velocity  $v_r$ , and pressure  $p$  along the radial distance  $r$  in the three-dimensional relativistic blast wave tests. The numerical computations are performed in a cube box with  $x = y = z = [0, 1]$  using  $256^3$  cells, and radial structures are measured along the main diagonal line  $x = y = z = 0$  to 1 at time  $t = 0.4$ . Numerical computations carried out with the general equation of state for an electron-proton gas and those done with an ideal gas equation of state with constant adiabatic index of  $\gamma = 5/3$  are marked using open and filled circles, respectively.

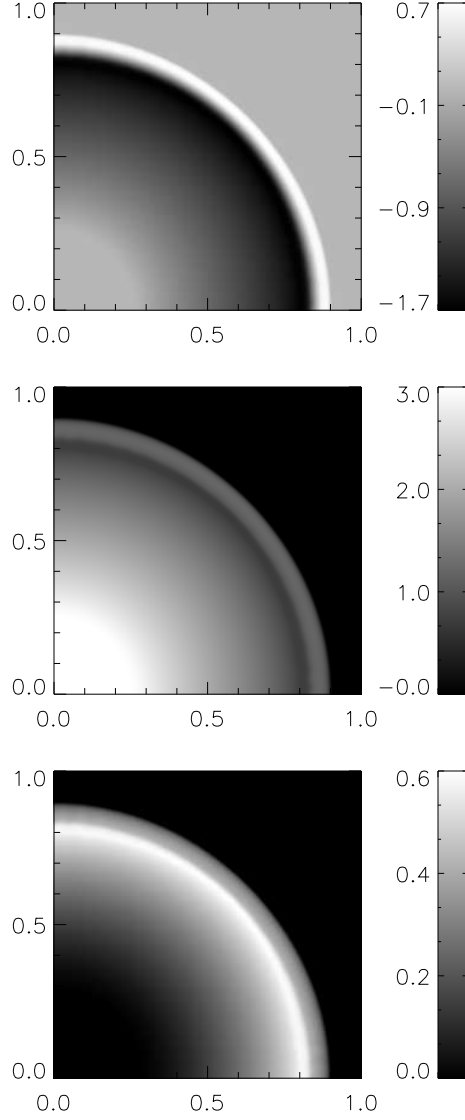


Fig. 7.— Images of rest mass density (top), pressure (middle), and Lorentz factor (bottom) in the three-dimensional relativistic blast wave test with the general equation of state for an electron-proton gas. The numerical computations are performed in a cube box with  $x = y = z = [0, 1]$  using  $256^3$  cells, and the images are shown in logarithmic scales on the plane  $x = 0$  at time  $t = 0.4$ .

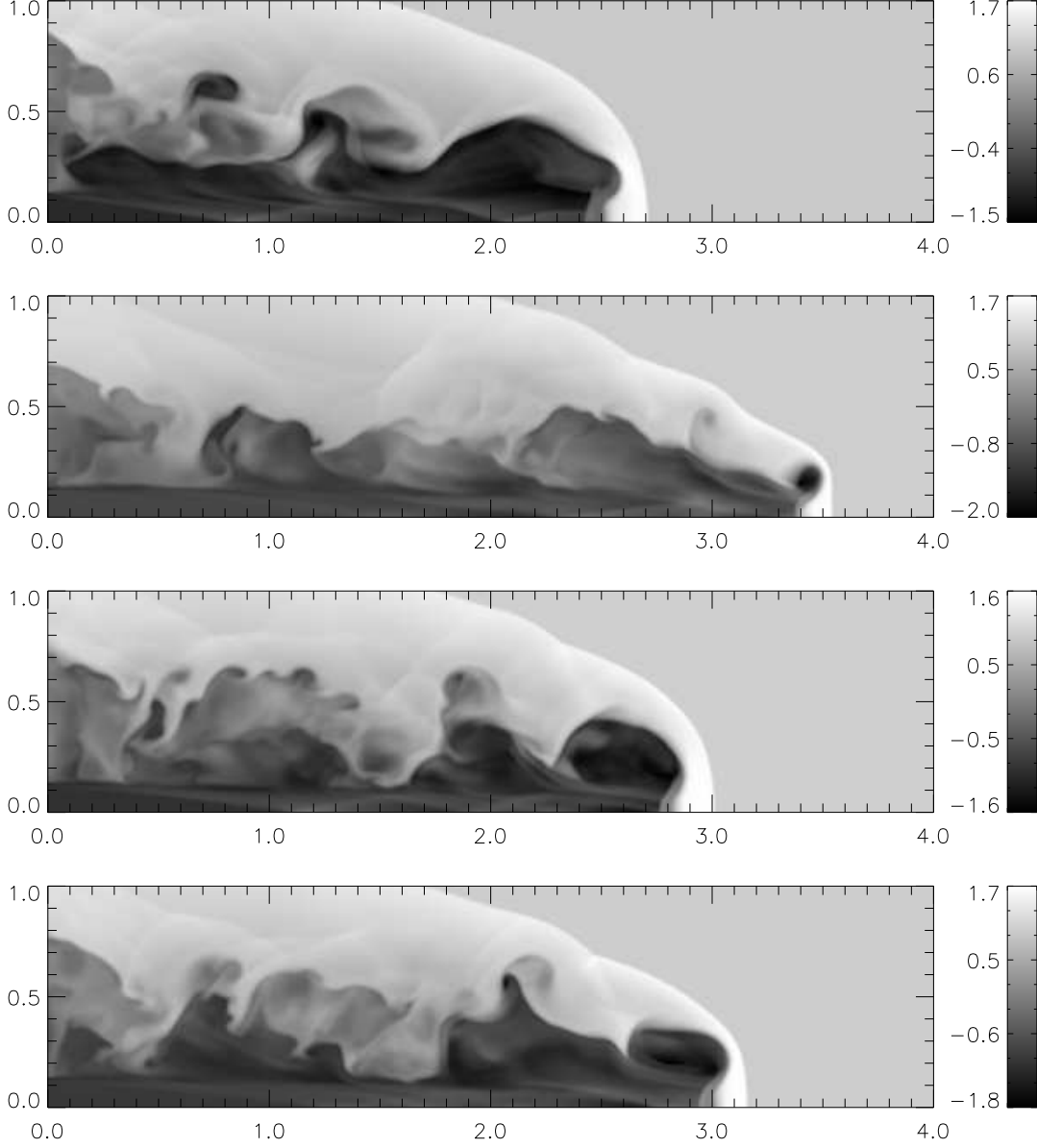


Fig. 8.— Images of the rest mass density for cases A to D (top to bottom) in the three-dimensional simulations of relativistic axisymmetric jets. The numerical simulations have been performed in the computational box with  $x = [0, 1]$ ,  $y = [0, 1]$ , and  $z = [0, 4]$  using  $128 \times 128 \times 512$  cells, and the images are shown in logarithmic scales on the plane  $x = 0$  at time  $t = 6$ .

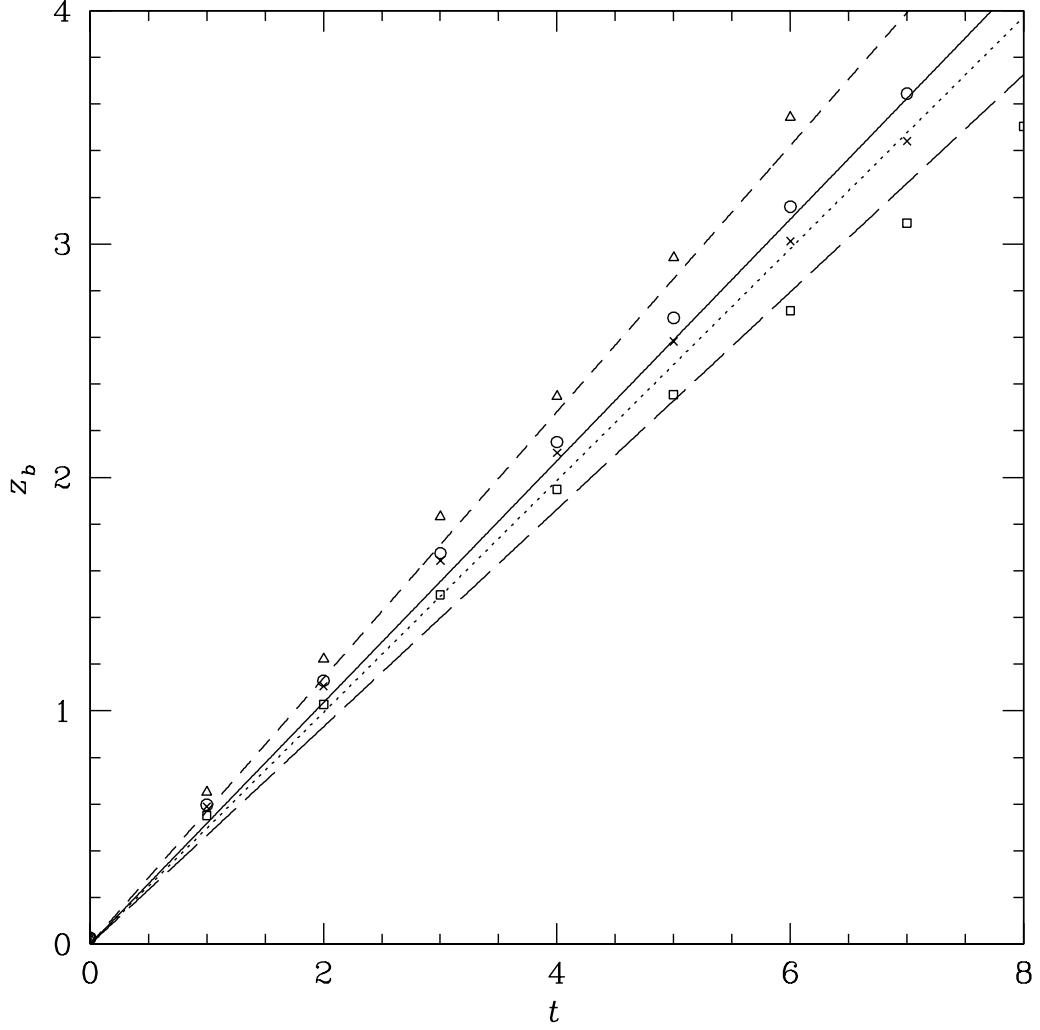


Fig. 9.— The position of the bow shock as a function of time for cases A to D in the three-dimensional simulations of relativistic axisymmetric jets. The numerical results are marked with squares, triangles, crosses, and circles for cases A to D at selected time intervals, respectively, and the long dashed, short dashed, dotted, and solid lines give the corresponding one-dimensional theoretical estimates.

Table 1. Norm Errors for Relativistic Shock Tube/Reflection Tests

Test	$\ E(\rho)\ $	$\ E(v_p)\ $	$\ E(v_t)\ $	$\ E(p)\ $
RST3a	4.96E−02	3.91E−03	0.00E+00	3.46E−02
RST3b	7.85E−02	2.38E−03	1.64E−03	3.11E−02
RST4a	4.43E−02	2.83E−03	0.00E+00	5.12E−01
RST4b	1.43E−01	2.20E−03	8.46E−04	4.21E−01
RSR5a	1.81E−01	2.33E−03	0.00E+00	2.61E−01
RSR5b	2.48E−01	2.92E−03	9.92E−04	6.91E−01

Note. — The test designation indicates relativistic shock tube (RST) and relativistic shock reflection (RSR) problems followed by corresponding figure numbers (3 to 5) and labels (a and b).

Table 2. Simulation Parameters for Relativistic Axisymmetric Jets

Case	$\eta$	$\Gamma_b$	$M_b$	$p_b$	EOS	$\chi$	$N_{\text{cell}}$	$t$
A	$10^{-2}$	7.1	2	$2.32 \times 10^{-2}$	5/3	-	$128 \times 128 \times 512$	8
B	$10^{-2}$	7.1	2	$6.94 \times 10^{-2}$	4/3	-	$128 \times 128 \times 512$	6
C	$10^{-2}$	7.1	2	$3.48 \times 10^{-2}$	$e^-e^+$	0.0	$128 \times 128 \times 512$	7
D	$10^{-2}$	7.1	2	$4.23 \times 10^{-2}$	$e^-p^+$	1.0	$128 \times 128 \times 512$	7

Note. — Here  $\eta$  is the density ratio of the beam to the ambient medium,  $\Gamma_b$  is the beam Lorentz factor,  $M_b$  is the beam Mach number,  $p_b$  is the uniform pressure in both the beam and the ambient medium, EOS is the type of equation of state,  $\chi$  is the relative fraction of proton and electron number densities,  $N_{\text{cell}}$  is the numerical resolution of the three-dimensional computational box, and  $t$  is the time out to which each simulation is followed.